Hindawi
Advances in Materials Science and Engineering
Volume 2022, Article ID 4091119, 14 pages
https://doi.org/10.1155/2022/4091119

Research Article

Synthesis, Structural, Spectroscopic, and Hirshfeld Surface Analysis, and DFT Investigation of Benzaldehyde Semicarbazone

N. Sudha,[1] S. Anbuselvi,[2] Sudhakar Jyothula,[3] A. Thiruppathi,[4] B. Vijayakumar,[5] Kartikeya Parmar,[6] G. Puthilibai,[7] and Leevesh Kumar[8]

[1]*PG & Research Department of Physics, Sri Sarada College for Women (Autonomous), Salem 636016, Tamil Nadu, India*
[2]*PG & Research Department of Chemistry, Sri Sarada College for Women (Autonomous), Salem 636016, Tamil Nadu, India*
[3]*Department of Electronics and Communications Engineering, Vignan's Institute of Engineering for Women, Visakhapatnam, Andhra Pradesh 530049, India*
[4]*Department of Mathematics, Panimalar Institute of Technology, Chennai, Tamil Nadu 600123, India*
[5]*Department of Chemistry, Panimalar Engineering College, Chennai, Tamil Nadu 600123, India*
[6]*Department of Mechanical Engineering, Nowgong Engineering College, Nowgong, Madhya Pradesh 471201, India*
[7]*Department of Chemistry, Sri Sairam Engineering College, Chennai, Tamil Nadu 600044, India*
[8]*Department of Construction Technology & Management, Ambo University, Ambo, Oromia, Ethiopia*

Correspondence should be addressed to Leevesh Kumar; leevesh.kumar@ambou.edu.et

Received 17 April 2022; Revised 30 April 2022; Accepted 18 May 2022; Published 16 June 2022

Academic Editor: Samson Jerold Samuel Chelladurai

By using slow evaporation, single crystals of BDSC (chemical name: 2-benzylidenehydrazine carboxamide) have been formed. A slow evaporation approach was used to generate BDSC single crystals. By using single-crystal XRD, the nonlinear characteristics of the material were studied. The presence of molecular groups was carefully examined using fundamental vibrational analysis. A Hirshfeld analysis was used to study the interactions between molecules. A series of UV-visible, photoluminescence, and VCD spectroscopic experiments were used to verify the optical characteristics of the material. In order to determine the electrical characteristics, dielectric investigations were carried out. Tests of Vickers hardness were used to measure mechanical strength. The SHG behaviour of the crystal was determined using the Kurtz–Perry method. To assess the molecule's thermal stability, all quantitative calculations were performed using the B3LYP approach with a basis function of 6-31 + G(d,p) and TG/DTA experiments.

1. Introduction

Molecular materials with greater hyperpolarizabilities have become a popular research area in recent years. Materials being strong optical and highly nonlinear have potential uses in data transfer, data storage, optical switching, and other fields as diverse as those mentioned above. Organic materials with significant NLO properties have already been found and synthesised. But just a handful of these were able to be crystallised and studied for second-order applications [1]. The crystallinity and stability of semicarbazone derivatives make them particularly attractive. Using acid and a base as a catalyst, semicarbazide reacts with aldehydes or ketones to produce semicarbazone derivatives [2–6].

Semicarbazide derivatives have become the subject of a large number of investigations in recent years. Because they might be useful in both industrial and biological applications, their functional and physical features are being studied [7, 8]. Thiosemicarbazones and thiosemicarbazone analogues are two of the most significant groups of Schiff basis compounds because they share the C=N functional group. As a result of their high nonlinearities and quick reflexes, organic NLO nanocrystals are preferable to inorganic ones in electrooptic devices. Delocalized-electron systems linking donors or acceptor groups increase asymmetric polarizability in organometallic NLO materials at the microscopic level [9]. Delocalized bonds are those where the electrons may travel across upwards of two nuclei at once. Organic

materials with the best nonlinear performance are constructed using molecular units with highly delocalized pi-electron moieties upon that ring. The existence of a delocalized cloud between the ring and chain causes asymmetry in polarizability. Because of the pi-electron transit over a bridge between donors and acceptors, polarisation is quite high. Using the bridge, donors and recipients may stay in touch via technological means.

Benzaldehyde is a highly symmetrical aromatic molecule with many hydrogen bonds. Its carboxylic group CHO in the para position of either the phenyl group was delocalized in order to create higher-order symmetry, which was accomplished by bond delocalization. Hyperpolarizability and second-order polarizability are both possible for the electron cloud that leads to the molecule. Because of this, when compound is crystallised, it acquires NLO characteristics [10]. NLO applications may benefit from Schiff base organic compounds, which have been identified to be promising materials [3, 11–14]. The characteristics of Schiff base crystal have been studied both experimentally and conceptually after a thorough review of the relevant literature.

2. Materials and Methods

2.1. Experimental Details: Synthesis. Merk supplies benzaldehyde (C_7H_6O) and semicarbazide hydrochloride (CH_6ClN_3O). Here are the steps for making the single-crystalline of benzaldehyde semicarbazone (the chemical name is 2 benzylidenehydrazine carboxamide). Alcohol and water are added until the mixture becomes somewhat cloudy, which may be eliminated with a few drops of alcohol. Then, 1.5 moles of sodium acetate and 0.1 moles of semicarbazide hydrochloride are added. In Figure 1, the reaction path is shown. About two hours of refluxing in boiling water and cooling the combination follow the well-shaken mixture. It is necessary to periodically recrystallize the white precipitate employing methanol as a solvent in order to achieve clear needle-shaped crystals, as illustrated in Figure 2, after washing with ethanol. Multiple characterisation approaches were used to verify the crystal's suitability for use in NLO systems.

2.2. Computational Details. The Gaussian 09 software package was used for all quantum chemical computations [15]. A DFT hybrid approach combining Becke's nonlocal three-parameter exchange with the Lee Young as well as Parr correlation (B3LYP) and the 6-31 + G(d,p) basis set was used to optimise the molecular geometries to meet conventional convergence requirements. No imaginary frequencies were identified for the wavenumbers derived by comparing them to potential energy minima. The title molecule's band gap energy may be determined using electromagnetic absorption spectra and frontier molecular orbitals. Reactive site charge concentrations were also measured using the B3LYP 6-31 + G(d,p) charge concentrations (d,p). Hyperpolarizability simulations have been used extensively to investigate the NLO feature of the aforementioned molecule.

3. Results and Discussion

3.1. An Investigation of the Crystal Structure and Molecular Structure. Analysis of single-crystal data from the MoK X-ray diffractometer Brucker Kappa APEXII revealed the crystalline phase of BDSC. A crystal of $0.300 \times 0.250 \times 0.200\,mm^3$ was used for the X-ray data collecting. In order to establish the BDSC's unit cell characteristics, we used least square methods and multiple reflections. Figures 3 and 4 show the ORTEP plot and indeed the optimised diagram, respectively. SHELX 97 was used to solve and improve the structure using the complete matrix least-squares approach [16]. Table 1 summarises the results of the analysis of the unit cell parameters. The produced crystalline is monomeric with such a quasispatial class P21/c, according to X-ray diffraction studies. (a) 11.9353, (b) 5.455, (C) 12.908, (D) 8.220, and (V) 820.2 3 are the lattice characteristics available throughout the research. A total of 6814 distinct reflections were observed in the wavelength of 3.229 to 24.994° in the range of *h*, *k*, and *l*, respectively. The *R* factor reduced to 1.183 after so many refining cycles.

The B3LYPP/6-31 + G(d,p) level of theory is being used to compute the geometrical characteristics of the title compounds. The symmetry of this molecule may be attributed to its position in the C_1 point group. The most significant feature of the compound was a good example of this type of binding energy and bond lengths. Tables 2 and 3 show the XRD and computationally optimised structural characteristics of the title molecule, respectively. The benzene ring in the molecule has had its chain replaced in ortho position. For C_3C_8 (1.408), the bond length is 0.17 nm longer than that of C_8C_7 (1.391 nm), C_4C_5 (1.395 nm), C_7C_8 (1.401 nm), and C_5–C_6 (1.395 nm). In order to maintain the force in the opposite direction between chains and rings, this increase to a maximum was extended. Because of bond interactions, the C_1 N_1 bond (1.393) was longer than the C_2 N_3 bond (1.286) [10]. It has been shown that the experimentally measured bond length in $N_2H(2A)$ is 0.86, whereas theoretical calculations place it at 1.017. Intermolecular interactions between molecules in the experimental investigation are to blame for this huge difference.

Between the chain and the ring, the bonding angle among $N_2C_2C_3$ was determined to be 122.77°. By virtue of the presence of attraction forces between this ring and NN of chain [11], this practically semicircular angle is creating another ring [12]. Because of the NH2 substitution on C, the bond length in $N_1C_1O_2$ is 123.7° higher. Bond angle in H(1A)N(1)H(1B) is 124°, a high value because of the electronegativity of amide group. Isolated gas-phase computations lead to minor discrepancies between experimental and theoretical results.

3.1.1. Hydrogen Bonding. It is evident from Table 4 that both weak and strong interactions exist throughout the molecule. The packing diagram with hydrogen bonding is depicted in Figure 5.

3.2. Hirshfeld Surface and Fingerprint Analysis. A Hirshfeld surface study [17] using the Crystal Explorer 3.1 tool [18–20]

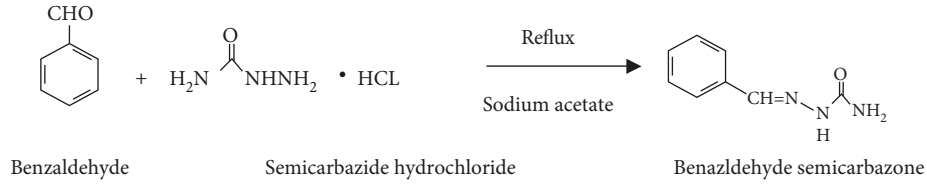

Figure 1: Reaction scheme of BDSC reflux sodium acetate benzaldehyde semicarbazone.

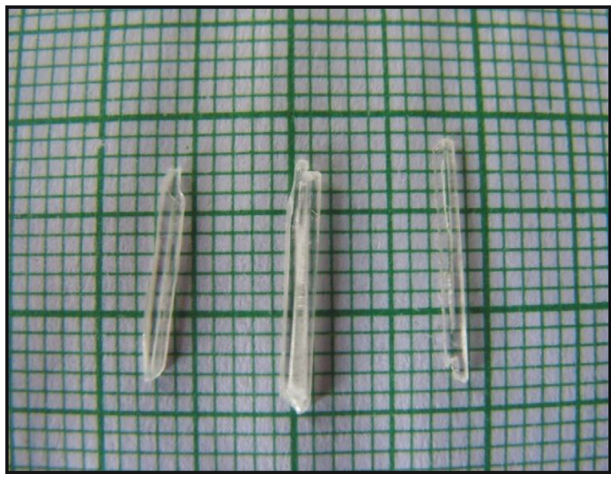

Figure 2: As-grown crystal of BDSC.

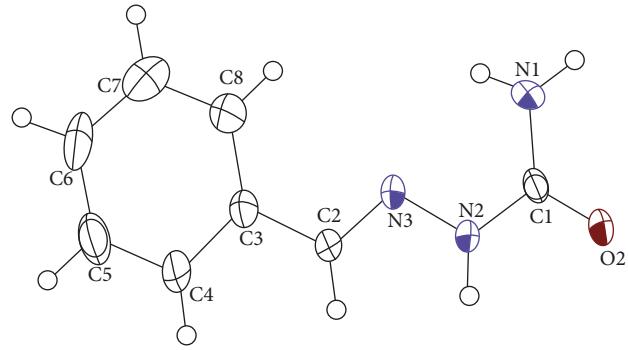

Figure 3: ORTEP diagram of $BDSC^-$ with the atomic numbering scheme.

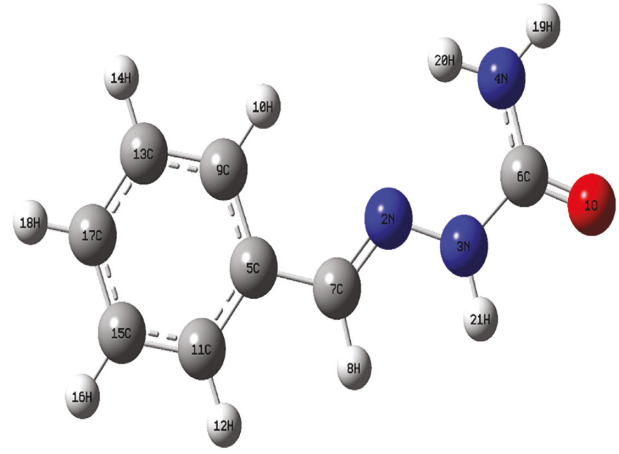

Figure 4: Optimised molecular structure of BDSC.

revealed the several types of interactions inherent in a crystal structure. The CIF files used to store the crystal structures were opened and imported. It is possible to create Hirshfeld surfaces by dividing space inside a crystal where the ratio between the electron densities of promolecules and procrystals is equal to 0 (d_{norm}). Figure 6 depicts the title compound's Hirshfeld three-dimensional d_{norm} surface. d_{norm}-coloured red hot patches on the surface are hydrogen bonds combining oxygen and nitrogen with nearby molecules that are very heated. It is possible to dissect the fingerprint scanning plots in order to emphasise a specific atom combination in close proximity. The H. . .H connections are by far the most common interaction inside the title compound, accounting for 43.7 percent of the total interactions. There are about 43.7 percent of the surface area of the Hirshfeld fingerprint plot accounted for by H contacts, with C. . .H interactions accounting for the second most prevalent kind of interaction. Other molecular interactions exist in addition to H. . .N and O. . .H. Figure 7 shows the molecule's numerous fingerprint areas.

3.3. Vibrational Analysis. The planes of its functional groups determine the organic compound's basic vibrations. The molecule was unravelled into 21 atoms using molecular symmetry (C_1), and there are 57 major modes of vibration that are active in the IR and Raman spectroscopies. As A57 represents, the full set of basic modes may be broken down into 37 in the plane vibrations of 20 out of the plane vibrations [21].

Table 5 shows the computed raw frequencies scaled down to match the measured wavenumber values. Figures 8 and 9 depict the experimental and simulated FT-IR and FT-Raman spectra, respectively. Realistic fundamental modes and the distinctive area of group frequencies were assigned and validated. There was a strong impact of surrounding attractive vibrations on all of the measured modes.

3.3.1. N–H Vibrations. The N–H absorption bands typically occur between 3400 and 3500 cm^{-1}. There are peaks at 3560 cm^{-1}, 3459 cm^{-1}, and 3287 cm^{-1} inside the NH2 stretching FT-Raman spectra in this work. The theoretical wavenumbers predicted by NH stretching have been confirmed empirically [22]. Molecular interactions within Schiff's base family of compounds, which generate high N–H bond forcing constants, are primarily focused on N and H. N–H deformation is responsible for IR peaks at

Table 1: Crystal data and structure refinement details of BDSC crystal.

Identification code	BDSC
Empirical formula	$C_8H_9N_3O$
Formula weight	163.18
Temperature	296(2) K
Wavelength	0.71073 Å
Crystal system	Monoclinic
Space group	$P2_1/c$
Unit cell dimensions	$a = 11.935(3)$ Å; $\alpha = 90^\circ$ $b = 5.4455(10)$ Å; $\beta = 102.341(9)^\circ$ $c = 12.918(3)$ Å; $\gamma = 90^\circ$
Volume	820.2(3) Å^3
Z	4
Density (calculated)	1.321 Mg/m^3
Absorption coefficient	0.092 mm^{-1}
F(000)	344
Crystal size	$0.300 \times 0.250 \times 0.200$ mm^3
Theta range for data collection	3.229 to 24.994°
Index ranges	$-14 \le h <= 14$, $-6 \le k \le 6$, and $-15 \le l \le 15$
Reflections collected	6814
Independent reflections	1444 [R(int) = 0.0504]
Completeness to theta = 24.994°	99.6%
Absorption correction	Semiempirical from equivalents
Max. and min. transmission	0.997 and 0.964
Refinement method	Full-matrix least-squares on F^2
Data/restraints/parameters	1444/0/121
Goodness of fit on F^2	1.183
Final R indices (I > 2sigma(I))	$R_1 = 0.0729$; $wR_2 = 0.1834$
R indices (all data)	$R_1 = 0.1091$; $wR_2 = 0.2067$
Extinction coefficient	n/a
Largest diff. peak and hole	0.233 and −0.262 e.Å^{-3}

1512 cm^{-1}, 1429 cm^{-1}, and 1491 cm^{-1} and Raman peaks at 1429 cm^{-1} and 1447 cm^{-1}. Experimental and theoretical values are quite similar.

3.3.2. C–H Vibrations. In the 3000–3100 cm^{-1} region, aromatic compounds often show C–H vibrational spectra. When it comes to this molecule, researchers have determined that the C–H stretching occurs at lengths ranging between 3065 and 2933 cm^{-1}. In IR and Raman, the wavenumber of C–H bending vibrations is 1139 cm^{-1}. In literature, these ideas are supported. It has been decided that the wavenumber range for C–H out of plane will be 850–1000 cm^{-1}. An out-of-plane C–H vibration at 998 cm^{-1} Raman and 995 cm^{-1} IR is designated. When it comes to the wavenumbers 881.1 cm^{-1}, 916.42 cm^{-1}, 961.61 cm^{-1}, or 1002.02 cm^{-1}, there seem to be theoretical values that match those obtained experimentally [23].

3.3.3. C=O Vibrations. Amides have C=O stretching vibrations of 1650–1670 cm^{-1} as a standard. This molecule possesses a C=O asymmetric stretching at 1689–1700 cm^{-1}, according to IR and Raman spectra. 1705 cm^{-1} is a good estimate for the region's highest point [24].

Table 2: Experiment and theoretical binding energies of BDSC crystals are compared.

Atoms with numbering	Experimental bond length (Å)	Theoretical bond length (Å)
O(2)-C(1)	1.22	1.244
N(3)-C(2)	1.28	1.273
N(3)-N(2)	1.35	1.369
N(2)-C(1)	1.39	1.353
N(2)-H(2A)	1.01	0.860
N(1)-C(1)	1.36	1.322
N(1)-H(1A)	1.00	0.940
N(1)-H(1B)	1.00	0.860
C(3)-C(8)	1.40	1.384
C(3)-C(4)	1.40	1.387
C(3)-C(2)	1.46	1.448
C(2)-H(2)	1.09	0.930
C(8)-C(7)	1.39	1.375
C(8)-H(8)	1.08	0.930
C(4)-C(5)	1.39	1.372
C(4)-H(4)	1.08	0.930
C(7)-C(6)	1.40	1.370
C(7)-H(7)	1.08	0.930
C(5)-C(6)	1.39	1.373
C(5)-H(5)	1.08	0.930
C(6)-H(6)	1.08	0.930

3.3.4. Ring Vibrations. The peaks at 1312 cm^{-1}, 1293 cm^{-1}, or 1161 cm^{-1} in this investigation are attributed to the C–C stretching vibrations. The benzaldehyde semicarbazone group bridge causes the wavenumber to change to the lower wavelength region. Vibrations of bending are assigned using the Gauss View and Veda software, in and out. 525 cm^{-1}, 625 cm^{-1}, 628 cm^{-1}, 692 cm^{-1}, 758 cm^{-1}, 856 cm^{-1}, and 611 cm^{-1} are all in-plane bending vibrations in IR and Raman. As per Inverse's Theory, the theoritical values are between 543 cm^{-1} and 881 cm^{-1}. Theoretically, at 507 cm^{-1} and 498 cm^{-1}, an out-of-plane bending occurs at 457 cm^{-1}.

3.3.5. C=N, C–N, and N–N Vibrations. For C=N stretching vibrations, there is a great deal of power inside the 1600–1490 cm^{-1} range [25]. Here, the infrared (IR) and Raman (Raman) vibration bands at 1600 or 1604 cm^{-1} are all in action, respectively. Because of its impressive exhibition, the imidazole group was able to retain a strong presence. Additionally, magnetic binding CN stretching may be seen [26], in addition to the 1382–1266 cm^{-1} values. In this condition, the IR achieves its greatest values at 1354 cm^{-1} as well as 1346 cm^{-1}, or the conceptual assignments are in excellent accord with the literature on the subject. These two Raman peaks, located at 264 cm^{-1}and 123 cm^{-1}, are caused by in-plane and out-of-plane vibrations, respectively. A very rare nuclear link exists between the azine group and the nucleus of another azine group. In this way, the NLO is connected to the rest of the globe via this connection. An important discovery of the azine bond is the N–N stretching vibration, which occurs at a frequency of 1080 cm^{-1} as a rule. This stretching vibration is helped by the experimental spectrum's 1092 and 1123 cm^{-1} peaks, which contribute to the stretching vibration.

Table 3: Bond angles in BDSC crystals: comparison of measured and computed values.

Atoms with numbering	Experimental bond angle (deg)	Theoretical bond angle (deg)
C(2)-N(3)-N(2)	118.08	115.918
C(1)-N(2)-N(3)	122.58	119.720
C(1)-N(2)-H(2A)	115.47	119.000
N(3)-N(2)-H(2A)	121.92	120.000
C(1)-N(1)-H(1A)	120.57	120.000
C(1)-N(1)-H(1B)	117.12	116.000
H(1A)-N(1)-H(1B)	120.76	124.000
C(8)-C(3)-C(4)	118.72	118.525
C(8)-C(3)-C(2)	122.51	122.181
C(4)-C(3)-C(2)	118.70	119.386
O(2)-C(1)-N(1)	124.93	123.773
O(2)-C(1)-N(2)	119.94	118.870
N(1)-C(1)-N(2)	115.11	117.621
N(3)-C(2)-C(3)	122.77	122.000
N(3)-C(2)-H(2)	120.60	119.000
C(3)-C(2)-H(2)	116.61	119.000
C(7)-C(8)-C(3)	120.35	120.325
C(7)-C(8)-H(8)	120.45	119.816
C(3)-C(8)-H(8)	119.18	119.818
C(5)-C(4)-C(3)	120.76	120.707
C(5)-C(4)-H(4)	119.64	119.702
C(3)-C(4)-H(4)	119.76	119.745
C(6)-C(7)-C(8)	120.40	120.615
C(6)-C(7)-H(7)	119.90	119.729
C(8)-C(7)-H(7)	119.60	119.782
C(6)-C(5)-C(4)	120.01	120.237
C(6)-C(5)-H(5)	120.19	119.919
C(4)-C(5)-H(5)	119.78	119.920
C(7)-C(6)-C(5)	119.60	119.621
C(7)-C(6)-H(6)	120.14	120.223
C(5)-C(6)-H(6)	120.20	120.224

Table 4: Hydrogen bonds for BDSC (Å and °).

D-H...A	d(D-H)	d(H...A)	d(D...A)	<(DHA)
N(1)-H(1A)...O(2)#1	0.94(4)	1.99(4)	2.913(4)	166(4)
N(2)-H(2A)...O(2)#2	0.86(5)	2.05(5)	2.914(4)	177(4)

Symmetry transformations used to generate equivalent atoms: #1 $-x, y+1/2, -z+3/2$; #2 $-x, -y, -z+2$.

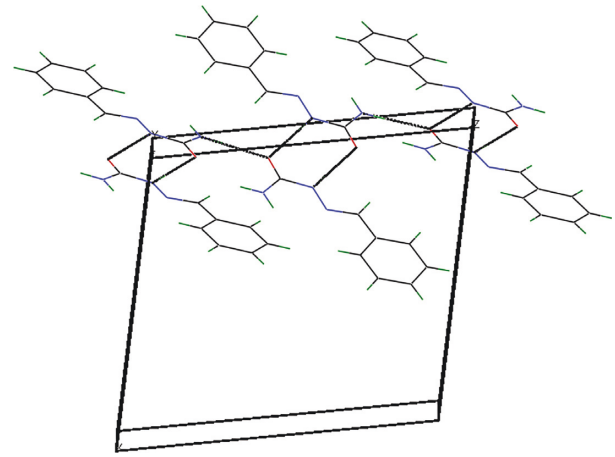

Figure 5: The BDSC's b-axis packing diagram.

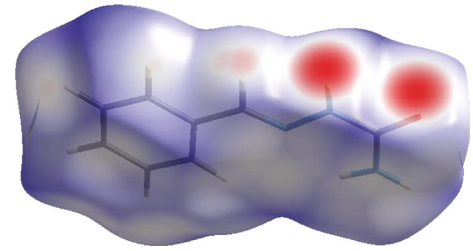

Figure 6: Hirshfeld surfaces mapped with d_{no}.

3.4. VCD Spectrum. VCD is an expansion of circular dichroism spectroscopic to the infrared and near-infrared regions. For example, the VCD gives two-dimensional structural information as ligand groups are mutually aligned. Figure 10 shows the molecule's VCD spectral profile. According to such left and right circular polarisation, the spectrum was generated from a value of zero, and the strength of the absorption was increased on the positive and negative sides. Although the absorption intensity on the two sides of the VCD spectrum is normally unequal, amalgamation was significantly more likely on the right side in this instance. The C=N, C=C, C=O, CC, NN, and CN stretching vibrations and NH and CH in bending vibration wavenumbers are all in the middle IR region, which includes both linear and circle vibrational polarisation bands. The organic molecules were active in all of these vibrational bands, which supports the induction of NLO activity.

3.5. UV-Visible NIR Spectral Analysis. In order to be used in optical applications, NLO materials must have a large transparency window in the UV-visible spectrum. Its UV-visible spectrum ranged from 200 to 1100 nanometers. It is shown in Figures 11(a) and 11(b) that perhaps the BDSC crystalline does have a reduced cut-off wavelength of 195 nanometers. To confirm that its wide transparency range inside the display area is a crucial quality for frequency doubling, a linear extrapolation of the chart's quadratic element indicated that such glass's band gap energy was 6.3 eV.

Absorption at 296.17 nm, 267.22 nm, and 231.76 nm is all n^* transitions inside the moment of density functional theory (TD-DFT) of the UV-Vis spectrum, which is estimated to use the time-dependent density functional (TD-DFT). In the imine group, these changes take place. Because the quartz UV crystal zone can easily be seen in this image, all changes take place inside this region. This point of view was essential in order to produce optical pulses with second-order harmonics. A reduction in wavelength causes an increase in absorption energy [27]. This is evidence that the frequency has doubled. Oscillator strength (f) and excitation energies, as well as spectral Figure 11(c) assignments, are reported in Table 6.

3.6. Photoluminescence Spectral Analysis. At room temperature, we measured the BDSC single-crystal photoluminescence emission spectrum using a Perkin Elmer LS45

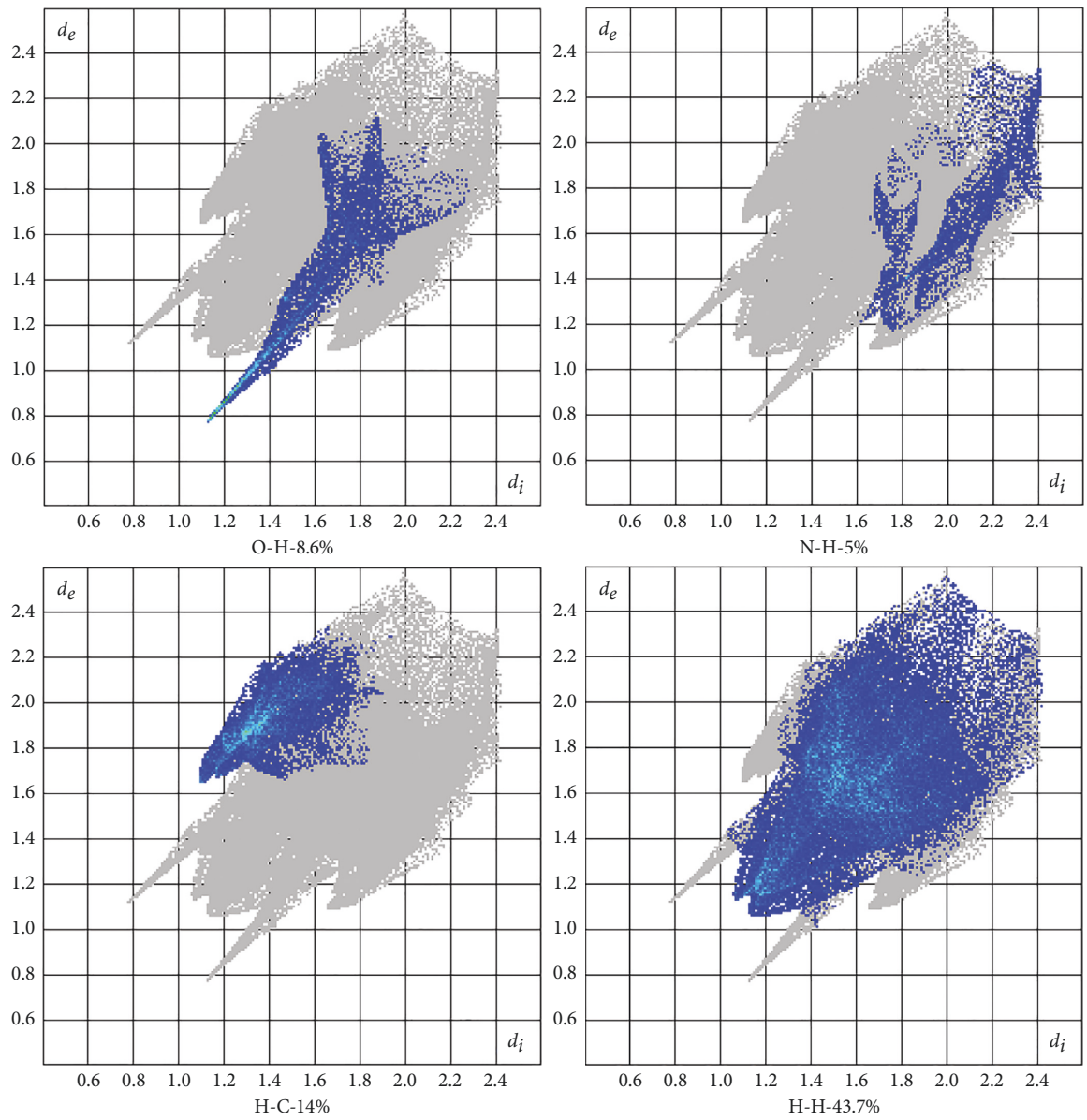

Figure 7: Fingerprint plots of BDSC O–H 8.6%; N–H 5%; H–C 14%; H–H 43.7%.

spectrophotometer to get the graph displayed in Figure 12. Since the material was excited at 344 nm, an optical emission spectrum may be seen. Spectra show a sharp peak at 405 nm in the violet emission band. Fluorescence emission from the BDSC crystal is yellow and orange in hue, with a maximum peak at 608 nm. Because of this, the BDSC crystal is an excellent choice for optical applications.

3.7. Electrical Properties. An important feature of the dielectric analysis is its potential to provide information on the electrical characteristics of a material medium in relation to temperature and frequency. The material's capacity to store and transport electric charges may be assessed using the results of this research.

When crystals are made of insulating materials, their dielectric characteristics are linked to their electrooptic properties [28–30]. Low dielectric constant materials are needed in the micro- and electronic sectors. A digital LCRZ metre is used to measure the BDSC crystal's dielectric constant from 50 Hz to 200 kHz at normal temperature. Figure 13(a) depicts the relationship between log frequency and dielectric constant (r). BDSC has fewer flaws, as seen by the decreasing dielectric constant with increasing frequency. Higher frequencies show a reduction in dielectric loss, proving that BDSC may be employed in NLO applications.

Figure 13(b) depicts the relationship between dielectric loss and logarithmic frequency. Thus, the reduced dielectric loss of BDSC crystals indicates high optical quality crystals with fewer flaws, which is critical for nonlinear optical.

3.8. Microhardness Study. There must be enough mechanical strength in a material to be employed in industry for gadget manufacture. Vickers microhardness experiments were used

Table 5: Observed and calculated frequencies of BDSC.

S. no.	Observed frequencies (cm^{-1})		Calculated frequencies with B3LYP/6-31 + G(d,p) (cm^{-1})				% potential energy distribution (PED)
	Infrared	Raman	Unscaled frequency	Scaled frequency	IR intensity	Raman activity	
1	3560		3760	3595	0.7659	1.5048	νNH (99)
2	3459	3460	3615	3456	0.1433	0.0312	νNH (99)
3	3287		3534	3379	1.4570	1.4557	νNH (100)
4			3217	3074	0.1030	0.4494	νCH ring (92)
5	3065	3065	3207	3066	137.4842	2.3004	νCH ring (88)
6			3195	3054	14.7837	1.6807	νCH ring (77)
7			3185	3045	88.2081	2.3036	νCH ring (84)
8	2991	3000	3176	3036	0.6092	2.5476	νCH ring (78)
9	2933		3055	2921	6.8617	0.9202	νCH ring (100)
10	1689	1700	1784	1705	0.7274	0.0053	νCO (69); νCN (10)
11	1600	1604	1681	1601	33.1229	2.2488	νCN (67)
12		1573	1649	1576	88.5832	0.6276	νCC (69); βHCC (19)
13			1622	1551	15.4648	0.4435	νCC(40); βCCC (10)
14	1512	1492	1597	1527	31.8174	2.5021	βHNH (85)
15	1407	1491	1535	1467	19.0095	0.7020	νCC (13); βHCC (49); βCCC (13)
16	1429	1447	1504	1436	5.5326	5.7416	βHNN (70); βHCC (10); νCN (11)
17			1482	1417	1.1242	5.4090	βHCC (46); βHNN (15); νCC (23)
18	1354	1340	1408	1346	3.3070	2.0524	βHNC (30); βCON (16); βHNN (15); νCN (42)
19	1320		1382	1321	5.5934	0.0033	βHNC (48); βHNN (36); νCN (10)
20	1313	1312	1364	1303	10.1936	0.1747	βHCC (82); νCC (12)
21	1231	1232	1336	1277	42.9585	2.2388	βHCC (54); νCC (11)
22			1255	1200	0.0076	0.6345	νCC (49); βHCN (14); βHCC (11)
23		1161	1201	1148	4.3953	4.4117	βHCC (74); νCC (11)
24	1139	1139	1185	1132	0.3840	3.0523	βHCC (75); νCC (10)
25	1125	1122	1176	1123	17.2308	4.8393	νNN (56); βHNN (20)
26	1092		1105	1056	0.1215	0.1721	νCC (41); βHCC (40)
27		1027	1088	1040	7.2734	18.3573	βHNC (54); νCN (13)
28	995	998	1049	1002	0.2423	1.1051	νCC (38); βHCC (22); βCCC (22)
29	965	960	1013	967	0.1762	85.5561	βCCC (46); νCC (23)
30			1005	961	6.2585	21.2600	τHCCC (66)
31			997	953	53.6761	0.3305	νCN (61)
32	947	950	985	942	7.0485	8.0354	τCCCH (81); τCCCC (14)
33			958	916	192.4667	136.3333	τHCNN (84)
34	856		922	881	0.6602	23.3469	τHCNN (92)
35			862	823	0.4412	80.9352	βCCC (32); νCC (19); βCCN (11)
36		820	855	817	28.3527	231.2089	τHCCC (97)
37	758		769	735	26.0776	64.6505	τHCCC (62); τCCCC (26)
38	692		743	709	0.1671	9.6972	δONNC (89)
39	668		702	671	18.9057	11.2138	τCCCC (44); τHCCC (41)
40	628		675	645	392.2790	3.4835	βCNN (45); βCCC (21)
41	600	611	633	605	18.0072	16.0599	βCCC (80)
42	580		614	586	167.1896	96.4836	βCNN (31); βCCC (24)
43	525		569	543	4.1280	18.3418	τHNCN (79)
44		505	531	507	345.1094	18.1174	βOCN (56)
45			522	498	2.9364	173.7363	δCCCC (66); τHCCC (13)
46	457		474	452	3.3875	1076.5380	τHNCN (82)
47			435	416	41.0981	1069.4464	βCNN (71)
48			415	396	731.6637	117.6310	τCCCC (81); τHCCC (15)
49		300	315	302	48.0756	73.0887	τCCNN (73)
50			289	276	7.9175	38.3422	νCC (27); βCCN (24)
51		264	269	257	0.0153	100.6765	δCCCC (64); τHNCN (14)
52		215	221	210	18.9075	108.9664	βCNN (78)
53			162	154	22.1948	232.6288	τHNCN (78); δCCCC (12)
54	123	122	117		6.8263	131.6087	δCCCC (77)
55		90	78	75	13.9160	256.1877	βCNN (89)

Table 5: Continued.

S. no.	Observed frequencies (cm^{-1})		Calculated frequencies with B3LYP/6-31 + G(d,p) (cm^{-1})				% potential energy distribution (PED)
	Infrared	Raman	Unscaled frequency	Scaled frequency	IR intensity	Raman activity	
56			55	52	32.9872	142.6358	δCCCC (76)
57		30	37	35	107.5694	46.5144	τCNNC (85)

ν: stretching, β: bending, δ: out-of-plane bending, and τ: torsion.

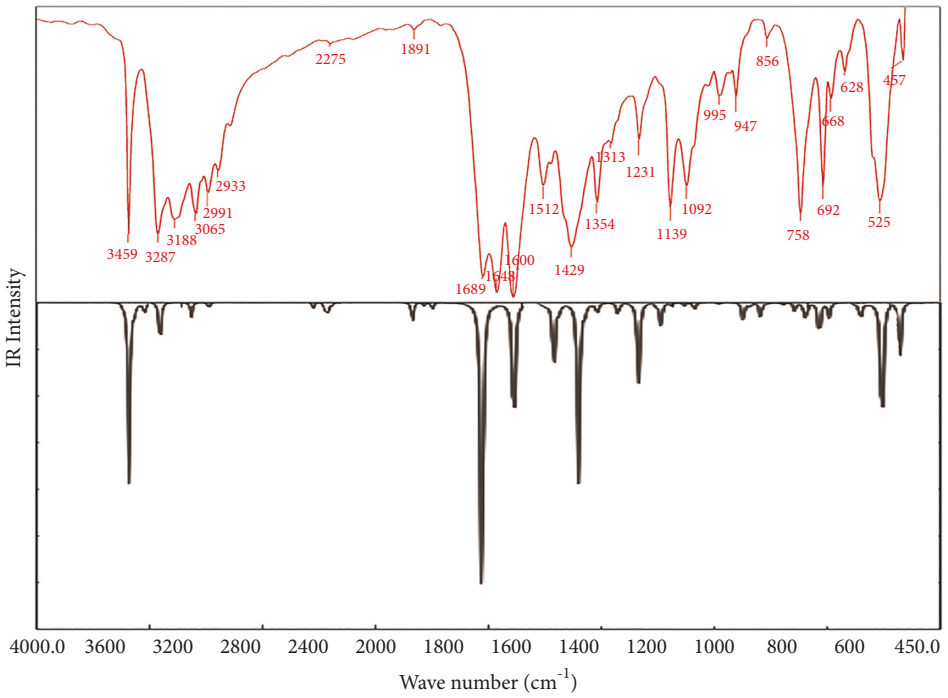

Figure 8: Experimental (a) and calculated (b) FT-IR spectra of BDSC.

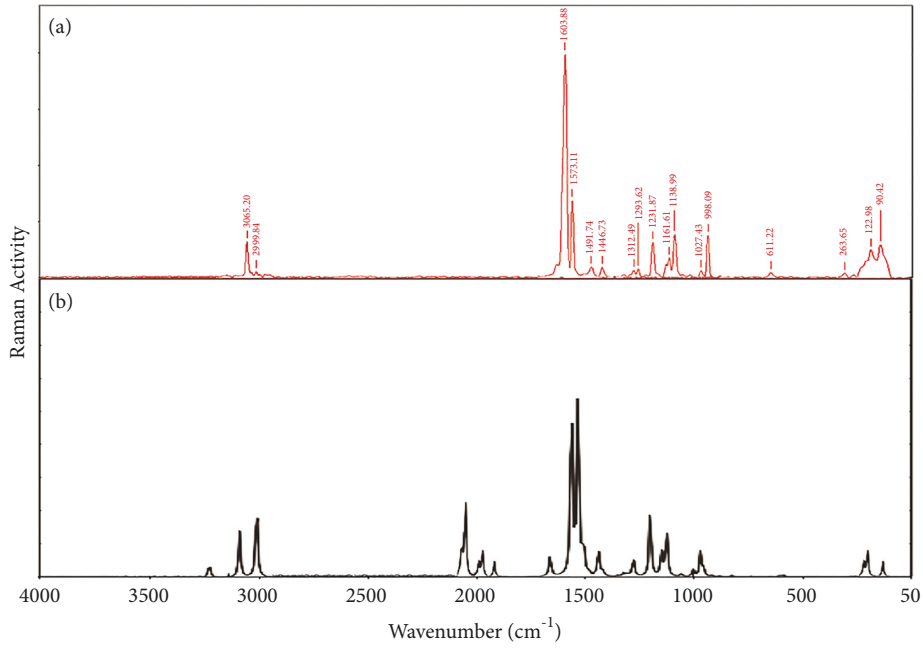

Figure 9: Experimental (a) and calculated (b) FT-Raman spectra of BDSC.

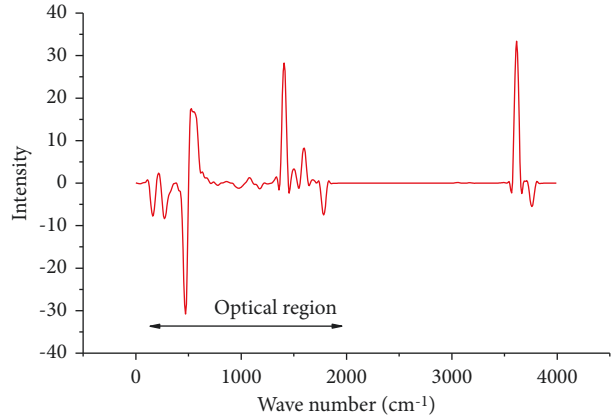

Figure 10: VCD spectrum of BDSC.

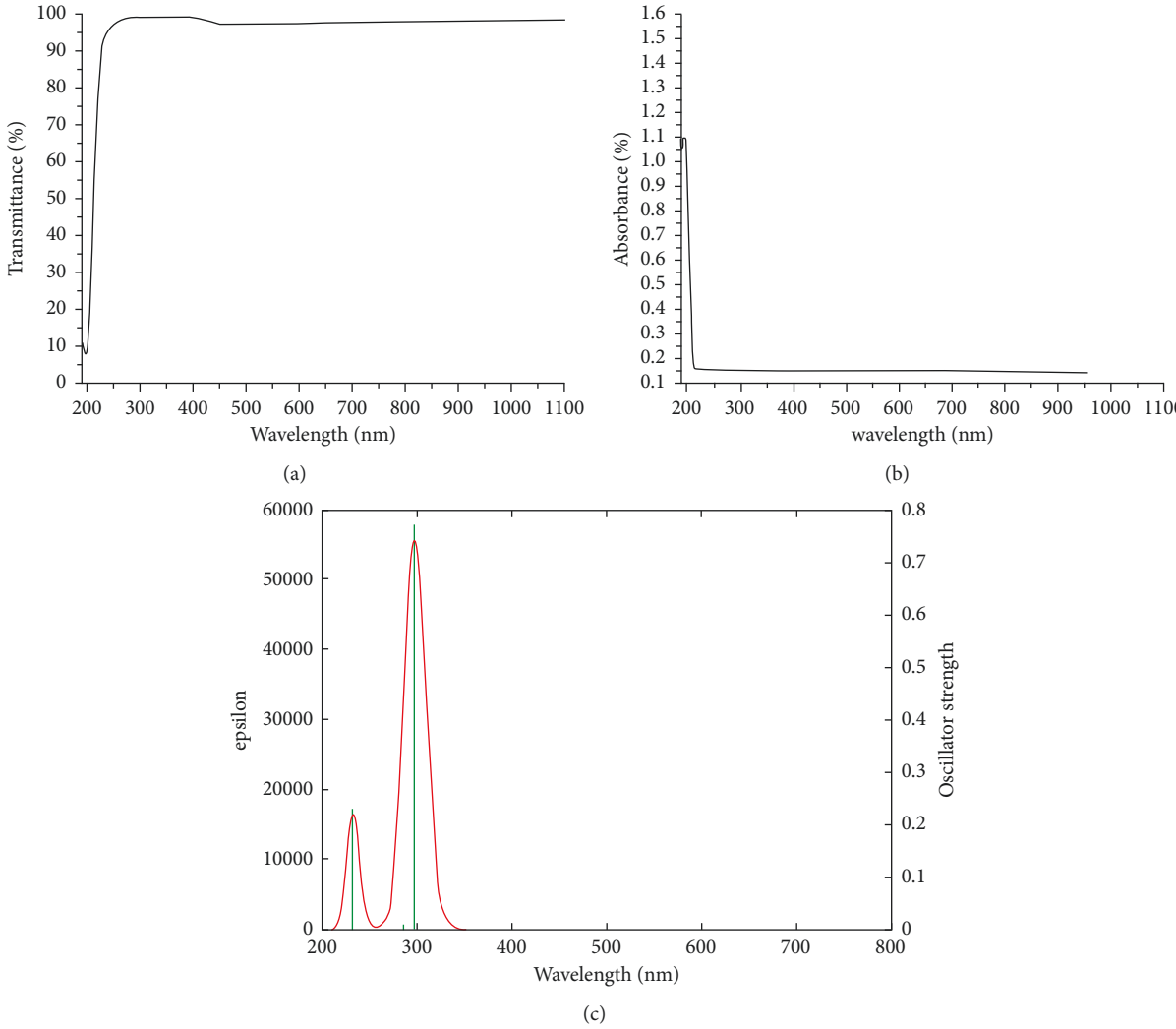

Figure 11: (a) UV-Vis transmittance. (b) UV-Vis absorption spectrum of BDSC spectrum of BDSC. (c) Theoretical UV spectra of BDSC.

to test the BDSC crystal's microhardness. The material's resistance to local deformation is measured by its hardness. An indenter load in kilogrammes (kg) and an imprint diagonal length in millimetres (mm) were used to determine the Vickers hardness number HV.

To illustrate this point, Figure 14(a) shows how the toughness of the HV changes along with the increasing pressure (p) from 25.1 to 100.0 grams. The line between log p and log d follows Meyer's index coefficient quite closely [31]. In Figure 14(b), the overall inclination of the graph is seen to

Table 6: BDSC electronic absorption spectrum values, both experimental and theoretical.

Excited state	Wavelength (λ) nm		Excitation energies (eV)	Oscillator strength (f)	Major contribution	Assignment
	Theoretical	Experimental				
S1	296.17	—	4.1863	0.7720	H $\longrightarrow$ L (98%)	$n \longrightarrow \pi^*$
S2	267.72	—	4.6311	0.0073	H-1 $\longrightarrow$ L-1 (97%)	$\pi \longrightarrow \pi^*$
S3	231.76	195	5.3497	0.2286	H-2 $\longrightarrow$ L-1 (86%)	$\pi \longrightarrow \pi^*$

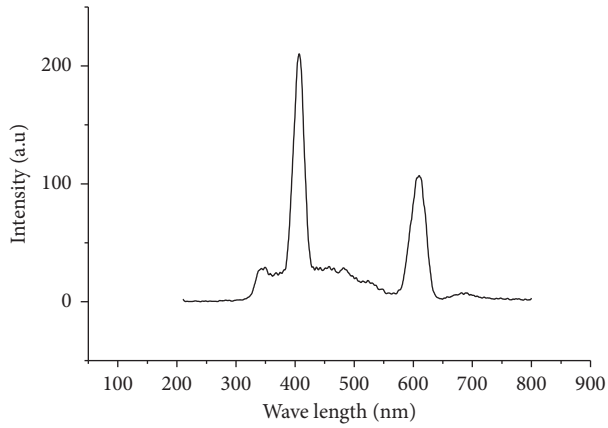

Figure 12: Photoluminescence emission spectra of BDSC.

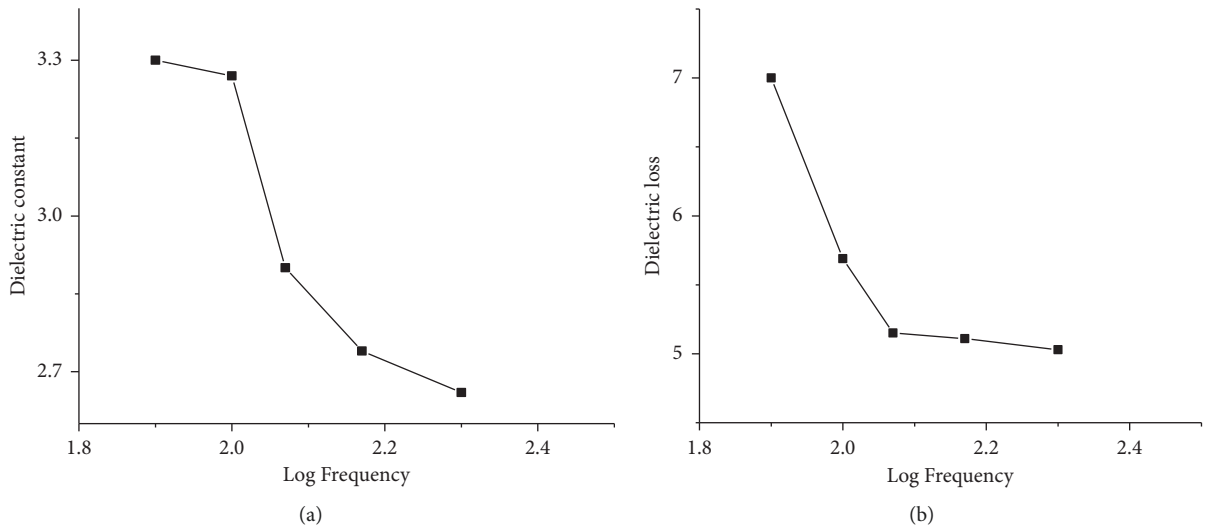

Figure 13: (a) Dielectric constant. (b) A logarithmic change changes with logarithmic frequency in dielectric loss.

be 2.9, which is the "n" number. As a result, BDSC crystal falls within the umbrella of soft materials.

3.9. Second Harmonic Generation Efficiency. To make optical storage systems, colour displays, and communication systems with high optical bandwidth and low dielectric constant, organic nonlinear optical crystals are in great demand. Background investigation of NLO materials may still benefit greatly from the Kurtz and Perry powder approach. The SHG production of the BDSC crystal was quantitatively measured using the method described above. A 0.68mj/pulse Nd:YAG laser operated at 1064 nm with an 8ns pulse width with a 10 HZ repetition rate. Using green irradiation from the sample, we were able to demonstrate that this molecule is a candidate for SHG applications because of its second harmonic signal. There were 9.2 mJ in production for urea and 4.5 mJ in output for the BDSC. This shows that the BDSC is 0.48 times larger than the regular urea.

3.10. Thermal Analysis. Figure 15 indicates that the produced material remains stable at room temperature up to 205°C, as can be seen from the TG/DTA graph. This proves that there is no solvent in the finished product. TGA estimates that 94% of the body's weight is lost throughout the decomposition process. At 205 degrees Celsius, an endothermic peak is seen due to the sample's melting point. An

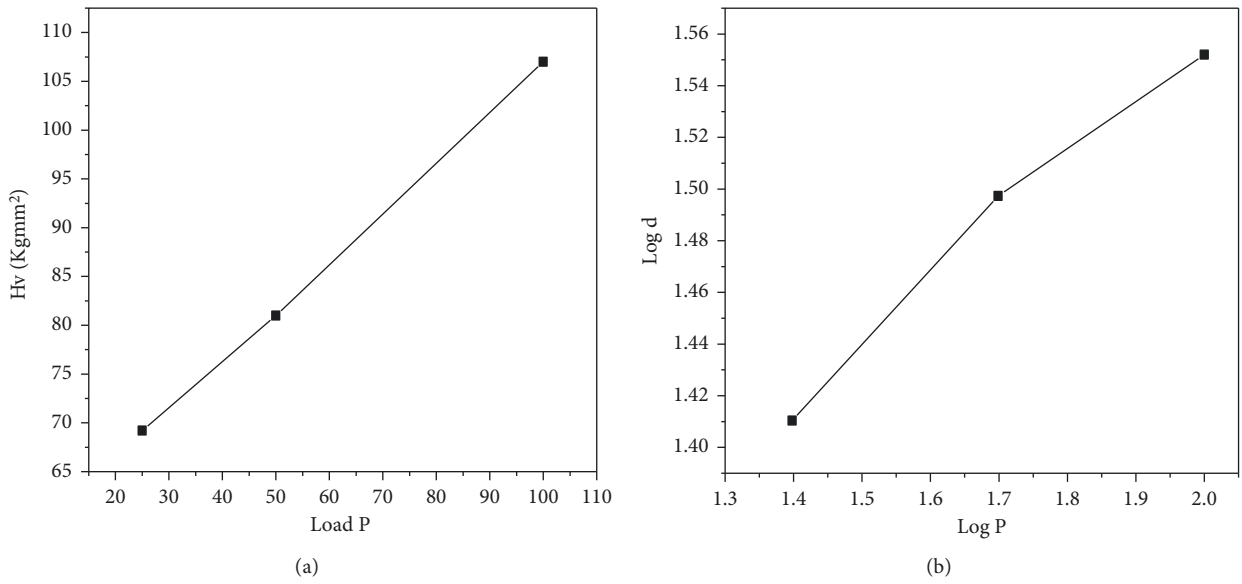

Figure 14: (a) Vickers microhardness. (b) Meyers index plot of BDSC plot of BDSC.

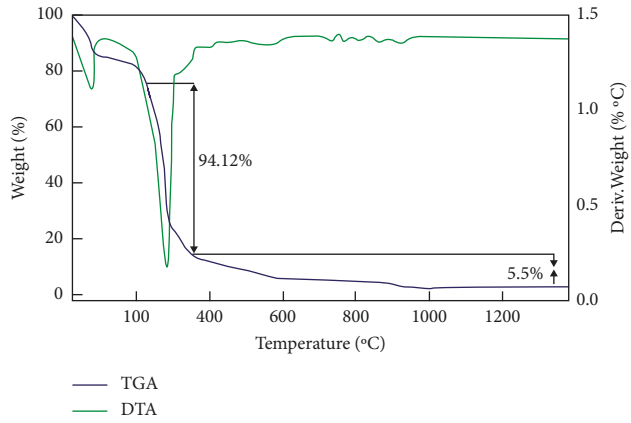

Figure 15: TG/DTA curves of BDSC.

Table 7: Based on DFT calculations using the 6-31 + G(d,p) basis set, values for the BDSC dipole moment, polarizability, and first-order hyperpolarizability were calculated.

Parameters	B3LYP/6-31G(d,p)	Parameters	B3LYP/6-31G(d,p)	Parameters	B3LYP/6-31G(d,p)
μx	0.844	α_{xx}	99.958	β_{xxx}	181.509
μy	0.882	α_{xy}	43.615	β_{xxy}	92.628
μz	1.097	α_{yy}	128.789	β_{xyy}	57.626
μ	**1.641**	α_{xz}	39.788	β_{yyy}	143.799
		α_{yz}	32.319	β_{xxz}	173.694
		α_{zz}	187.061	β_{xyz}	162.743
		$\boldsymbol{\alpha_{tot}}$	**138.602**	β_{yyz}	269.932
		$\boldsymbol{\alpha_{tot}}$ **esu**	$\mathbf{20.5409 \times 10^{-24}}$ **esu**	β_{xzz}	167.438
				β_{yzz}	231.553
				β_{zzz}	240.979
				β_{tot}	$\mathbf{7.975 \times 10^{-30}}$ **esu**

endothermic reaction at 205°C with a high degree of clarity suggests that the crystals created were of excellent quality.

3.11. Theoretical First-Order Hyperpolarizability. DFT has been used extensively to investigate crystals' NLO properties. Nonzero and ν values are more strongly influenced by the chemical's intermolecular hydrogen bonding. B3LYP/6-31 + G(d,p) basis set was used to determine a first-order particularly powerful and dipole moment using a finite field approach. The study of intermolecular interactions is often

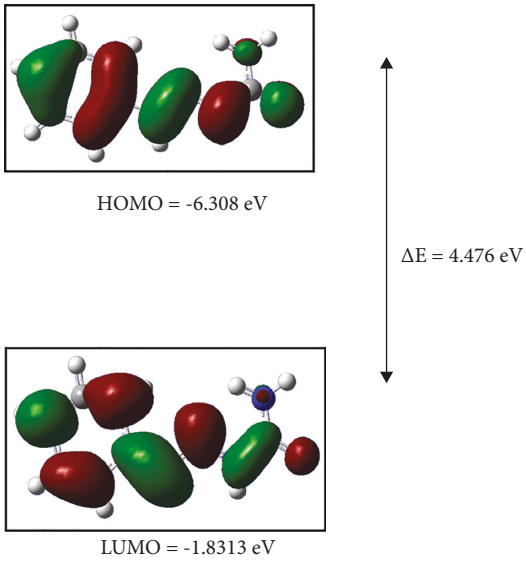

Figure 16: Frontier molecular orbitals of BDSC.

Table 8: Calculated molecular orbital parameters of BDSC employing 6-31 + G (d) basis set.

Parameters	BDSC (eV)
E_{HOMO}	−6.3085
E_{LUMO}	−1.8313
E_{HOMO}–E_{LUMO}	4.4772
Ionisation potential	6.3088
Electron affinity	1.8313
Chemical hardness (η)	2.2383
Softness (ζ)	0.4468
Electronegativity (χ)	4.0699
Electrophilicity index (ψ)	4.5540

carried out using molecular dipole moments as a technique. The larger the dipole moment is, the more intermolecular interactions will occur. Molecular interconnection is evident from the dipole moment of BDSC, which measures 4.172 Debye (D). For this compound, the theoretically estimated NLO values mentioned in Table 7 were used to compute the linear and first-order polarizability tensors. According to the data, BDSC's hyperpolarizability is 13.23 times more than urea's.

3.12. Frontier Molecular Orbital Analysis. Using the B3LYP/6-31 + G(d,p) exact same position in the Gaussian 09 programme, a HOMO-LUMO energy band gap was calculated. This material's interaction with other organisms is governed by the HOMO-LUMO boundary orbitals. A BDSC border molecular compound may be seen in the image above. C=O, C–N, N here on the NH2 group, or C–C bonds are determined to be homogeneous (HOMO) (benzene ring). C–C, C–N, or C–H bonds all have LUMOs that may be seen throughout them. Its HOMO-LUMO or energetic difference of a molecule is important for predicting its activity. Energy expenditures have been meticulously planned.

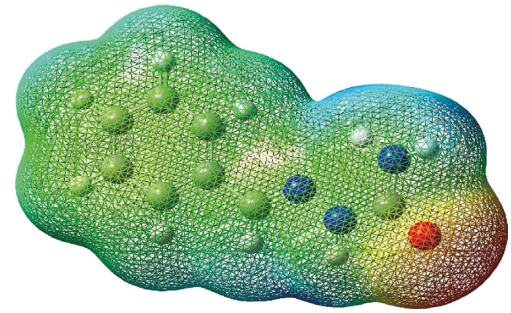

Figure 17: MESP map of BDSC.

$$\begin{aligned} \text{HOMO energy} &= -6.308\ \text{eV}, \\ \text{LUMO energy} &= -1.8313\ \text{eV}, \\ \text{HOMO} - \text{LUMO energy gap} &= 4.4767\ \text{eV}. \end{aligned} \tag{1}$$

When the electrochemical reaction transition and, subsequently, the nonlinear optical responses are allowed to proceed more easily, the HOMO-LUMO overlap is evident in these orbital topologies [32] (Figure 16). Charge transfer interactions among molecules and a dynamic component for NLO applications are explained by the reduction in the HOMO and LUMO energy gap. Because the molecule's theoretical value is assigned to its gas phase, the anticipated HOMO-LUMO energy gap is less than the ultraviolet light optical energy gap. Intermolecular forces, such as Vander Waals interaction in crystal field interactions, also affect the morphology of the solid-state structure. Table 8 includes a few more parameters, such as electron affinity, chemical hardness, softness, and the electrophilicity index, which are calculated and presented.

3.13. Electrostatic Potential on the Molecular Surface. With the use of electrostatic potential (MEP), molecular structure may be linked to physical properties. Molecule electrostatic potential (MEP) is a quantitative description of the molecule's electric potential (electrons + nucleus), its shape, size, and dipole moments. As a consequence, the reactive sites of molecules may be inferred from this map of the MEP surface. MEP diagram colours indicate an electron deficit or partial positive charge. Red indicates an electron-rich zone, whereas blue indicates an electrode-deficient or partly positive ion. Because oxygen and nitrogen have stronger negative potentials than carbon, electron shortage is created by an excess of potentiality in the BDSC molecule. Additionally, Figure 17 provides an overall view of how each of these molecules' molecular applied electric surfaces is connected, which provides an insight into how each of these molecules is wired. The MEP's surface may be used to observe electrophilic and nucleophilic reactions.

4. Conclusion

The information presented here expands our understanding of the manufacturing process for Schiff base benzaldehyde semicarbazone. After a single XRD, the crystal was found to be monomeric with such a P21 space group. All

microstructures in crystals may be explored using Hirshfeld surfaces. It was decided to investigate the functional groups of the molecule using FT-IR and FT-Raman spectroscopy. BDSC's nonlinearity is supported by its optical properties. The dielectric studies confirm the nonlinearity. The material is soft and pliable. In addition, chemical reactivity is shown using DFT simulations such as HOMO-LUMO. The hyperpolarizability of BDSC has been determined to be 13.23 times greater than that of urea. MEP has BDSC chemical reactive sites. The VCD spectrum confirms the presence of optical activity. A new method for producing optical materials can be seen in this paper that uses a Schiff base.

Data Availability

The data used to support the findings of this study are included within the article.

Conflicts of Interest

The authors declare that they have no conflicts of interest.

References

[1] C. S. Barrett and T. B. Massalski, *Structure of Metals: Crystallographic Methods, Principles, and Data*McGraw-Hill, New York, NY, USA, 1966.

[2] R. Ueda, J. B. Mullin, I. O. of Crystal Growth, and I. U. of Crystallography, *Crystal Growth and Characterization: Proceedings of the ISSCG2 Springschool*North-Holland Pub. Co, Japan, 1975.

[3] S. Janarthanan, Y. C. Rajan, P. R. Umarani, D. Jayaraman, D. Premanand, and S. Pandi, "Synthesis, growth, optical and thermal properties of a new organic crystal semicarbazone of p-anisaldehyde (SPAS)," *Indian Journal of Science and Technology*, vol. 3, 2010.

[4] T. W. Greene and P. G. M. Wuts, *Protective Groups in Organic Synthesis*Wiley, Hoboken, NJ, USA, 1999.

[5] J. R. Hanson, *Protecting Groups in Organic Synthesis*Sheffield Academic Press, Sheffield, UK, 1999.

[6] R. L. Shriner, *The Systematic Identification of Organic Compounds*A Laboratory Manual Wiley, Hoboken, NJ, USA, 1980.

[7] H. C. Yao and P. Resnick, "Azo-hydrazone conversion. III. The autoxidation of benzaldehyde phenylhydrazones," *Journal of Organic Chemistry*, vol. 30, no. 8, pp. 2832–2834, 1965.

[8] R. Fusco and F. Sannicolo, "New rearrangement of arylhydrazones in polyphosphoric acid: formation of diaryl ethers 4," *Journal of Organic Chemistry*, vol. 46, no. 1, pp. 90–92, 1981.

[9] S. N. Pandeya, P. Yogeeswari, and J. P. Stables, "Synthesis and anticonvulsant activity of 4-bromophenyl substituted aryl semicarbazones," *European Journal of Medicinal Chemistry*, vol. 35, no. 10, pp. 879–886, 2000.

[10] N. Moorthy, P. C. J. Prabakar, S. Ramalingam, G. V. Pandian, and P. Anbusrinivasan, "Vibrational, NMR and UV-visible spectroscopic investigation and NLO studies on benzaldehyde thiosemicarbazone using computational calculations," *Journal of Physics and Chemistry of Solids*, vol. 91, pp. 55–68, 2016.

[11] N. Moorthy, P. C. J. Prabakar, S. Ramalingam, M. Govindarajan, S. J. Gnanamuthu, and G. V. Pandian, "Spectroscopic analysis, AIM, NLO and VCD investigations of acetaldehyde thiosemicarbazone using quantum mechanical simulations," *Journal of Physics and Chemistry of Solids*, vol. 95, pp. 74–88, 2016.

[12] R. Ramesh Babu, N. Vijayan, R. Gopalakrishnan, and P. Ramasamy, "Growth and characterisation of benzaldehyde semicarbazone (BSC) single crystals," *Journal of Crystal Growth*, vol. 240, no. 3-4, pp. 545–548, 2002.

[13] A. Arfan and M. Rukiah, "Crystal structures of crotonaldehyde semicarbazone and crotonaldehyde thiosemicarbazone from X-ray powder diffraction data," *Acta Crystallographica Section E Crystallographic Communications*, vol. 71, no. 2, pp. 168–172, 2015.

[14] S. Janarthanan, R. Sugaraj Samuel, Y. C. Rajan, P. R. Umarani, and S. Pandi, "Spectral and thermal characterization of grown organic single crystal," *Journal of Thermal Analysis and Calorimetry*, vol. 109, no. 1, pp. 69–72, 2012.

[15] G. M. Sheldrick, *SHELXL-97, Progress Crystal-Structure Refinement*, Univ. Gottingen, Ger, Göttingen, Germany, 1997.

[16] J. J. McKinnon, D. Jayatilaka, and M. A. Spackman, "Towards quantitative analysis of intermolecular interactions with Hirshfeld surfaces," *Chemical Communications*, vol. 37, p. 3814, 2007.

[17] M. S. S. K. Wolff, D. J. Grimwood, J. J. McKinnon, M. J. Turner, and D. Jayatilaka, "Crystal-explorer," 2012, https://wiki.crystalexplorer.net/quick-start.

[18] H. Khanam, A. Mashrai, N. Siddiqui et al., "Structural elucidation, density functional calculations and contribution of intermolecular interactions in cholest-4-en-3-one crystals: i," *Journal of Molecular Structure*, vol. 1084, pp. 274–283, 2015.

[19] Y.-H. Ma, S.-W. Ge, W. Wang, and B.-W. Sun, "Studies on the synthesis, structural characterization, Hirshfeld analysis and stability of apovincamine (API) and its co-crystcal (terephthalic acid: apovincamine = 1:2)," *Journal of Molecular Structure*, vol. 1097, pp. 87–97, 2015.

[20] S. M. Kumar, B. C. Manjunath, G. S. Lingaraju, M. M. M. Abdoh, M. P. Sadashiva, and N. K. Lokanath, "A Hirshfeld surface analysis and crystal structure of 2′-[1-(2-fluoro-phenyl)-1H-tetrazol-5-Yl]-4-Methoxy-Biphenyl-2-Carbaldehyde," *Crystal Structure Theory and Applications*, vol. 02, no. 03, pp. 124–131, 2013.

[21] J. Mohan, *Organic Spectroscopy Principles and Applications*Narosa, New Delhi, Delhi, India., 2004.

[22] S. Rashev and D. C. Moule, "Variational study on the vibrational level structure and IVR behavior of highly vibrationally excited S0 formaldehyde," *Spectrochimica Acta Part A: Molecular and Biomolecular Spectroscopy*, vol. 87, pp. 286–292, 2012.

[23] G. Socrates, *Infrared and Raman Characteristic Group Frequencies: Tables and Charts*, Wiley, Hoboken, NJ, USA, 2001.

[24] R. M. Silverstein, F. X. Webster, and D. Kiemle, *Spectrometric Identification of Organic Compounds*, Wiley, Hoboken, NJ, USA, 2005.

[25] N. Sundaraganesan, J. Karpagam, S. Sebastian, and J. P. Cornard, "The spectroscopic (FTIR, FT-IR gas phase and FT-Raman), first order hyperpolarizabilities, NMR analysis of 2,4-dichloroaniline by ab initio HF and density functional methods," *Spectrochimica Acta Part A: Molecular and Biomolecular Spectroscopy*, vol. 73, no. 1, pp. 11–19, 2009.

[26] A. Dhandapani, S. Manivarman, S. Subashchandrabose, and H. Saleem, "Molecular structure and vibrational analysis on (E)-1-(3-methyl-2,6-diphenyl piperidin-4-ylidene) semicarbazide," *Journal of Molecular Structure*, vol. 1058, pp. 41–50, 2014.

[27] S. N. Pandeya, V. Mishra, P. N. Singh, and D. C. Rupainwar, "Anticonculsant activity of thioureido derivatives of

acetophenone semicarbazone," *Pharmacological Research*, vol. 37, no. 1, pp. 17–22, 1998.

[28] D. S. Chemla and G. Darst, *Nonlinear Optical Properties of Organic Molecules and Crystals: Ill*Acadamic Press, Cambridge, MC, USA, 1987.

[29] S. Boomadevi, H. P. Mittal, and R. Dhansekaran, "Synthesis, crystal growth and characterization of 3-methyl 4-nitropyridine 1-oxide (POM) single crystals," *Journal of Crystal Growth*, vol. 261, no. 1, pp. 55–62, 2004.

[30] H. Reyes, B. M. Muñoz, N. Farfán et al., "Synthesis, crystal structures, and quadratic nonlinear optical properties in a series of push-pull boronate derivatives," *Journal of Materials Chemistry*, vol. 12, no. 10, pp. 2898–2903, 2002.

[31] R. N. Singh, A. Kumar, R. K. Tiwari, P. Rawat, D. Verma, and V. Baboo, "Synthesis, molecular structure and spectral analysis of ethyl 4-formyl-3,5-dimethyl-1H-pyrrole-2-carboxylate thiosemicarbazone: a combined DFT and AIM approach," *Journal of Molecular Structure*, vol. 1016, pp. 97–108, 2012.

[32] R. A. Meyers, "Wiley InterScience (online service)," *Encyclopedia of Analytical Chemistry: Applications, Theory, and Instrumentation*, Wiley, Hoboken, NJ, USA, 2000.